ACS OMEGA

Article

Cite This: ACS Omega 2018, 3, 1329−1337

Sn-Doped Rutile TiO_2 Hollow Nanocrystals with Enhanced Lithium-Ion Batteries Performance

Shilong Jiao,[†,∥] Gang Lian,*[,†,§,∥] Laiying Jing,[†] Zhenghao Xu,[†] Qilong Wang,[‡] Deliang Cui,*[,†] and Ching-Ping Wong*[,§]

[†]State Key Lab of Crystal Materials and [‡]Key Laboratory for Special Functional Aggregated Materials of Education Ministry, School of Chemistry & Chemical Engineering, Shandong University, Jinan 250100, P. R. China

[§]School of Materials Science and Engineering, Georgia Institute of Technology, Atlanta, Georgia 30332, United States

Supporting Information

ABSTRACT: Hollow structures and doping of rutile TiO_2 are generally believed to be effective ways to enhance the performance of lithium-ion batteries. Herein, uniformly distributed Sn-doped rutile TiO_2 hollow nanocrystals have been synthesized by a simple template-free hydrothermal method. A topotactic transformation mechanism of solid $TiOF_2$ precursor is proposed to illustrate the formation of rutile TiO_2 hollow nanocrystals. Then, the Sn-doped rutile TiO_2 hollow nanocrystals are calcined and tested as anode in the lithium-ion battery. They deliver a highly reversible specific capacity of 251.3 mA h g^{-1} at 0.1 A g^{-1} and retain ∼110 mA h g^{-1} after 500 cycles at a high current rate 5 A g^{-1} (30 C), which is much higher than most of the reported work.

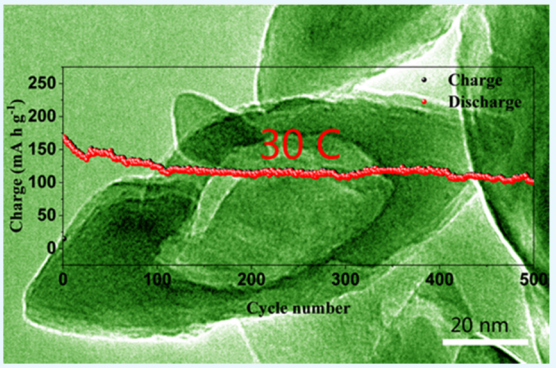

1. INTRODUCTION

Development of high-performance lithium-ion batteries (LIBs) with wider work-temperature range, increased power density, and improved safety is highly demanded for future portable electronics and electric and hybrid vehicles.[1,2] Among various anode materials, TiO_2 has been considered as a potential anode candidate because of excellent Li-ion insertion/extraction reversibility with a neglectable volume expansion (3−4%) and a high operating voltage (>1 V vs Li^+/Li),[3−7] which reduces the excessive formation of solid electrolyte interphase (SEI) on anodes. In addition, TiO_2 is suitable for large-scale application because of its natural abundance, low cost, and nontoxicity.[8] Therefore, various polymorphs of TiO_2 (rutile, anatase, brookite, and bronze) have recently been studied as active materials for LIBs.[9] Among them, rutile TiO_2 is the most thermodynamically stable form.[10] Unfortunately, the lithium storage performance of rutile TiO_2 is still unsatisfactory, which is mainly derived from its highly anisotropic diffusion of Li^+ in bulk rutile (10^{-6} cm^2 s^{-1} along *c*-axis; 10^{-15} cm^2 s^{-1} along *ab*-plane)[11,12] and intrinsic limitation of storage capacity.[13,14] To enhance the rate capacity, enormous researches have been devoted to overcome its intrinsic disadvantages. One of those effective approaches focuses on preparing nanosized hollow rutile TiO_2 to shorten the transport path for both Li^+ ions and electrons in TiO_2 nanostructures.[15−17] The hollow interior also provides an extra free space that can alleviate the structural strain and accommodate the volume variation. It is associated with the repeated Li^+ ions insertion/extraction process, leading to the improved cycling stability.[18,19] Another effective strategy is to dope alien atoms (e.g., C, N, B, Fe, Nb, Mn, Sn, etc.) in TiO_2.[8,20−27] The doping method is attracting more attention because it not only benefits the electron-transfer process but also offers more channels for Li^+ diffusion due to the slightly modified lattice of the doped TiO_2.[24] Sn^{4+} is taken as an example because the theoretical capacity of SnO_2 (≈790 mA h g^{-1}) is much higher than that of rutile TiO_2.[28,2928,29] Sn(IV)-ion doping into rutile TiO_2 at the atomic level can anticipate improved electrochemical performance with increased capacity and higher retention.

Although many kinds of rutile TiO_2 nanostructures with different morphologies have been intensively investigated, synthesis of hollow nanocrystals is still a great challenge by a template-free method.[30] Herein, we report the preparation of Sn-doped rutile TiO_2 hollow nanocrystals by a facile template-free hydrothermal method. When measured as anode in lithium-ion batteries, the Sn-doped rutile TiO_2 hollow nanocrystals exhibit a greatly improved electrochemical performance, including a high specific capacity, an excellent rate property, and a long-life cycling stability. This material showed a much enhanced capacity of 251.3 mA h g^{-1} after 150 cycles under 0.1 A g^{-1}. Furthermore, a reversible capacity of ∼110 mA h g^{-1} after 500 cycles at 5 A g^{-1} (30 C) can still be retained and the Coulombic efficiency (CE) maintained almost 100% during the 500 cycles, confirming the excellent rate property of the Sn-

Received: September 10, 2017
Accepted: October 24, 2017
Published: January 31, 2018

DOI: 10.1021/acsomega.7b01340
ACS Omega 2018, 3, 1329−1337

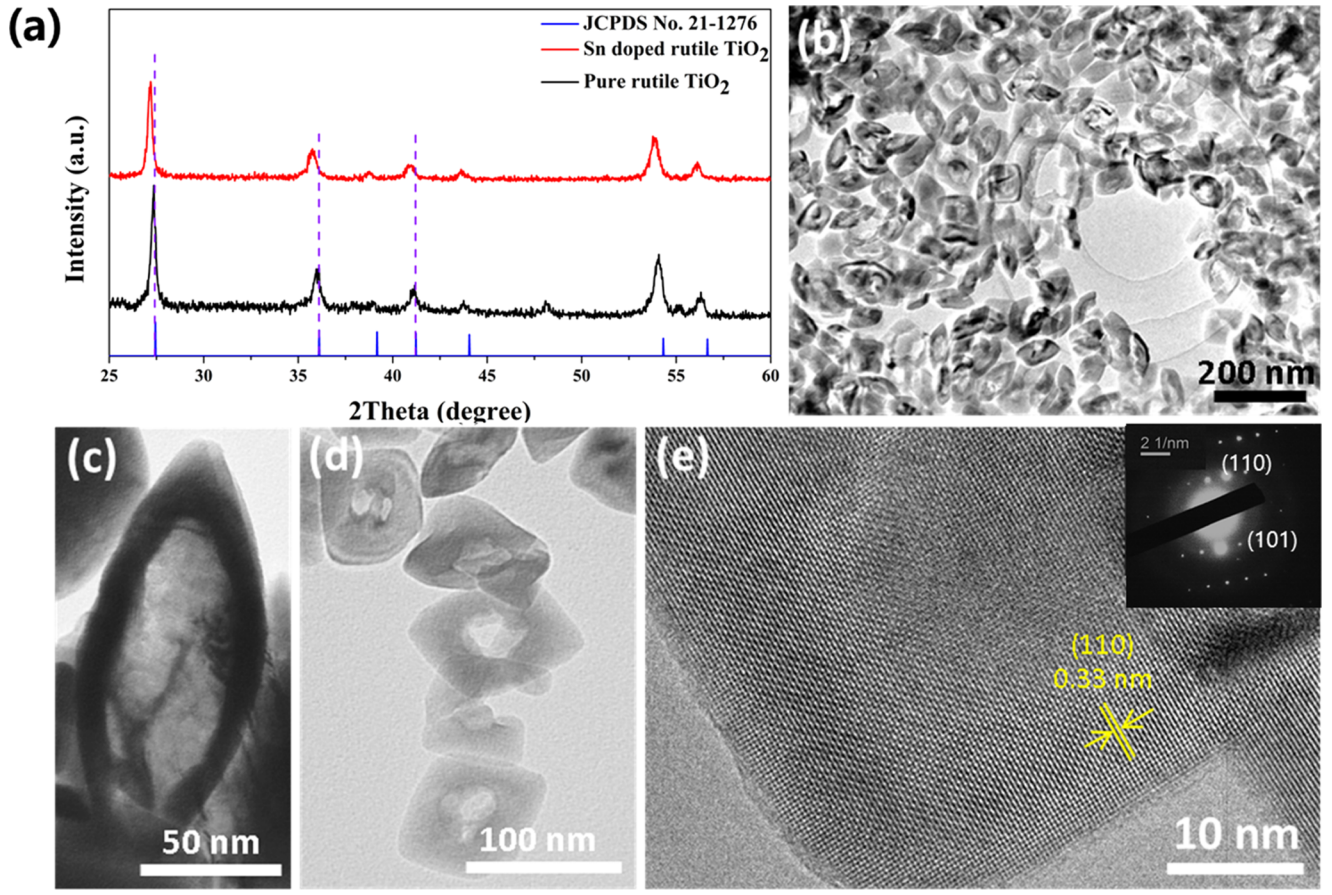

Figure 1. (a) XRD pattern of the Sn-doped rutile TiO_2 sample and the pure rutile TiO_2. (b) TEM image of the Sn-doped rutile TiO_2 hollow nanocrystals. (c) Magnified TEM image of single Sn-doped rutile TiO_2 hollow nanocrystal. (d) Top view of the Sn-doped rutile TiO_2 hollow nanocrystal. (e) HRTEM image of the Sn-doped rutile TiO_2 hollow nanocrystal. Inset is the corresponding SAED pattern of the nanocrystal.

doped rutile TiO_2 hollow nanocrystals. The excellent lithium-ion storage performance benefits from hollow nanostructures, high crystallinity, and uniform Sn-ion doping.

2. EXPERIMENTAL SECTIONS

2.1. Preparation of the Sn-Doped Rutile TiO_2 Hollow Nanocrystals. The Sn-doped rutile TiO_2 hollow nanocrystals were obtained via a facile template-free hydrothermal method. In a typical process, 4 mmol $SnCl_4{\cdot}5H_2O$ was dissolved in 20 mL tetrabutyl titanate (TBOT) and vigorously stirred for 10 min. 4.5 mL HF solution (30%) was then added drop by drop in it. The solution was then transferred into a 40 mL Teflon tube and sealed into the autoclave, which was heated to 200 °C for 24 h. The obtained products were washed several times with ethanol and water after cooling to the room temperature. Finally, they were annealed at 500 °C for 2 h to remove the impurities. To investigate its growth process, time-dependent experiments were carried out for 10, 18, and 24 h, respectively. In addition, different amounts (0, 1, 2, 4, 6, and 8 mmol) of $SnCl_4{\cdot}5H_2O$ were also introduced to illustrate the formation of pure Sn-doped rutile TiO_2 hollow nanocrystals.

2.2. Electrochemical Characterization. Electrochemical measurements were carried out by using LIR2032 coin cells.[31] The working electrode consisted of active material, acetylene black (super-P) and poly(vinylidene fluoride) with the weight ratio of 8:1:1. The assembly of the coin cells was performed in a glove box full of Ar. The Celgard 2400 film was used as separator. The electrolyte was composed of ethylene carbonate, dimethyl carbonate (DMC), and ethylene methyl carbonate, with the volume ratio of 1:1:1 as solvent and $LiPF_6$ as solute with the concentration of 1 mol L^{-1}. The counter electrode of the coin cells was mainly composed of pure lithium foil. The galvanostatic charge/discharge curve of the coin cells was obtained on a LAND Cell Test system in a setting voltage range (2001A, Wuhan, China). A CHI760D electrochemical working station was used to carry out the cyclic voltammetry (CV) tests in the same setting voltage range with the charge/discharge test rate of 0.2 mV s^{-1}. Electrochemical impedance spectroscopy (EIS) patterns were studied by using the same working station in the CV tests. The frequency range was set from 100 kHz to 0.01 Hz, with an amplitude of 5 mV. After the cycle performance test, the coin cells were disassembled and washed with dimethyl carbonate (DMC) to remove the electrolyte from the electrode surface. After that, the sample was dried at 80 °C for 24 h before examination.

2.3. Characterization Methods. X-ray powder diffraction (XRD) patterns of the as-obtained samples were recorded on a Rigaku D/Max-γ A X-ray diffractometer with the scanning rate of 4° min^{-1}. Morphologies of the samples were examined with scanning electron microscope (SEM, Hitachi S-4800), transmission electron microscope (TEM, JEOL H-7000), and high-resolution transmission electron microscope (HRTEM, JEOL JEM-2100). The element analysis was carried out by X-ray photoelectron spectrometer (XPS, ESCALAB 250). The Accelerated Surface Area and Porosimeter 2000 analyzer was

DOI: 10.1021/acsomega.7b01340
ACS Omega 2018, 3, 1329−1337

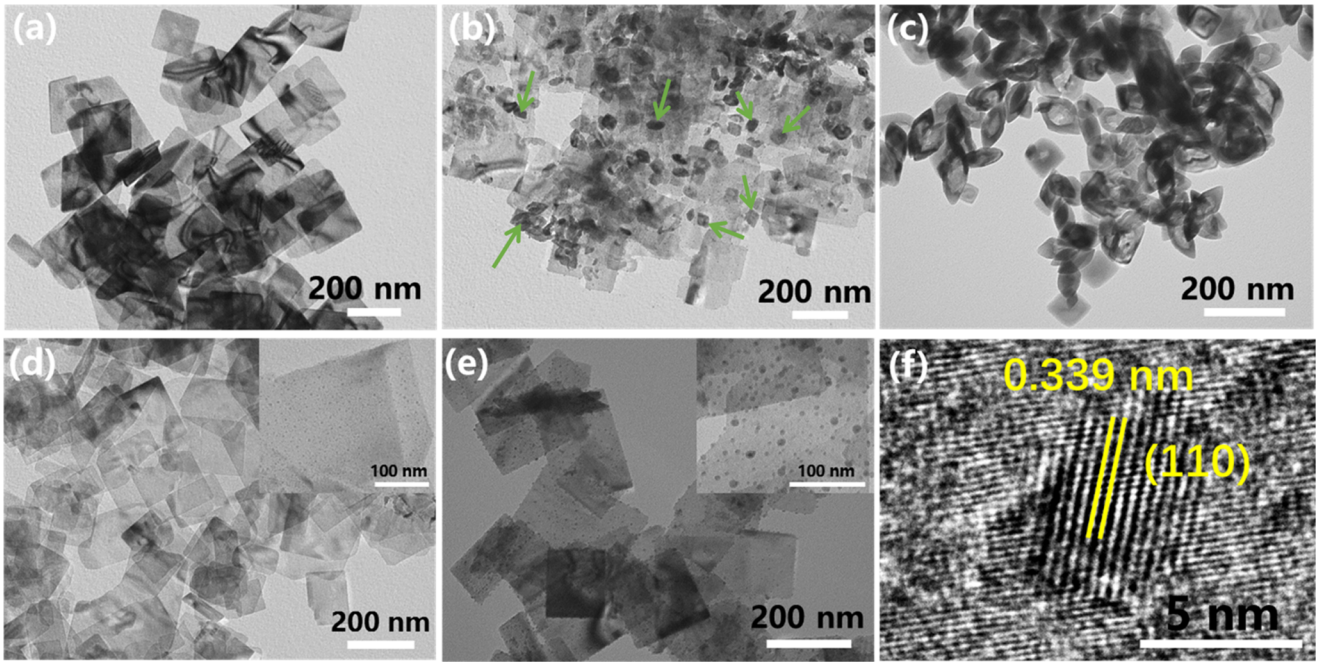

Figure 2. TEM images of TiO_2 samples synthesized with (a) 0 mmol, (b) 2 mmol, (c) 4 mmol, (d) 6 mmol, and (e) 8 mmol $SnCl_4{\cdot}5H_2O$; (f) HRTEM image of SnO_2 quantum dots from (e).

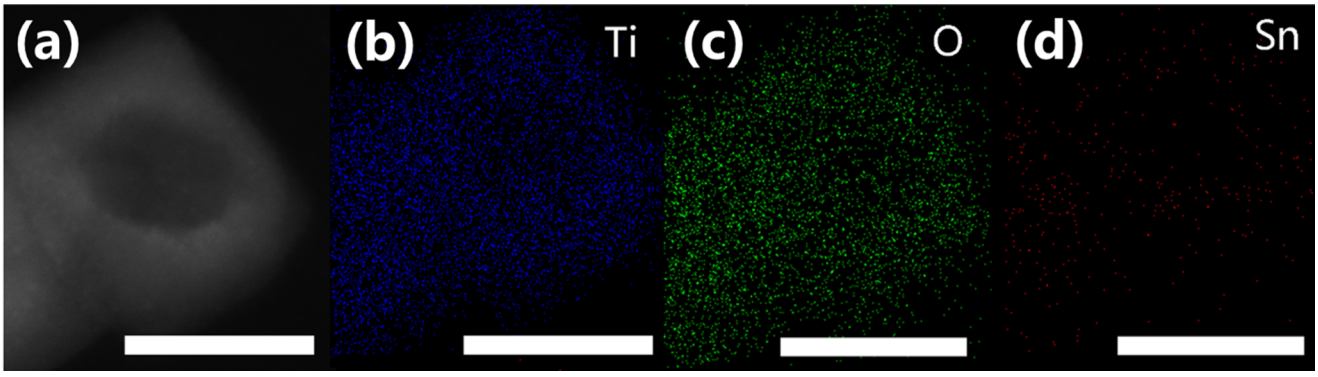

Figure 3. (a) STEM image of single Sn-doped TiO_2 nanocrystal. (b–d) EDS mappings of Ti, O, and Sn elements. The scale bar is 100 nm.

used to measure the Brunauer–Emmett–Teller specific surface area of the sample.

3. RESULTS AND DISCUSSION

The phase composition of Sn-doped TiO_2 sample was confirmed by XRD (Figure 1a). All of the diffraction peaks can be indexed to rutile TiO_2 (JCPDS No. 21-1276), and no other peaks corresponding to SnO_2 were observed in the XRD pattern, preliminary indicating effective doping of tin in rutile TiO_2 lattice. It is noted that the peaks slightly shifted to smaller angles, as observed by Rogach et al.[25,32] The lattice expansion is attributed to a substitution of the Ti site in the rutile by Sn due to a larger ionic radius of Sn^{4+} (55 pm) than that of Ti^{4+} (42 pm).[33] Figure 1b–d shows the typical TEM images of Sn-doped rutile TiO_2 with a size of 100–150 nm. The nanocrystals have clear hollow interior voids, with some holes on their surfaces (Figure S1), which is possibly derived from the etching of HF solution. The selected area electron diffraction (SAED) pattern corresponding to the single hollow nanocrystal demonstrates its single-crystalline nature (inset in Figure 1e). The HRTEM image exhibits clear lattice fringes, indicating high crystallinity of the nanocrystal (Figure 1e). The lattice spacing is ~0.33 nm, corresponding to the (110) plane of rutile TiO_2.[13]

Actually, when no Sn precursor was added to the starting solution, only anatase TiO_2 nanosheets were prepared (Figures 2a and S2). Incorporation of Sn element into TiO_2 lattice was accompanied with a phase transformation from anatase to rutile (Figure 2b,c). When 2 mmol $SnCl_4{\cdot}5H_2O$ was dissolved in TBOT, it is noticed that some hollow nanocrystals (labeled by arrow in Figure 2b) appeared in the sample of anatase TiO_2 nanosheets. The analysis of phase composition reveals the coexistence of anatase and rutile TiO_2 (Figure S2). Furthermore, the anatase nanosheets were completely converted into Sn-doped rutile hollow nanocrystals with the injection of 4 mmol $SnCl_4{\cdot}5H_2O$, which was also supported by the XRD pattern in Figure S2. Only rutile TiO_2 sample was synthesized in the condition. However, excessive Sn precursor easily resulted in phase separation of TiO_2 and SnO_2. As shown in Figure 2d–f, a large amount of SnO_2 nanocrystals uniformly dispersed on the surfaces of TiO_2 nanosheets. The emergence of TiO_2 nanosheets instead of hollow nanocrystals means that the rutile TiO_2 returned back to anatase phase. The

DOI: 10.1021/acsomega.7b01340
ACS Omega 2018, 3, 1329–1337

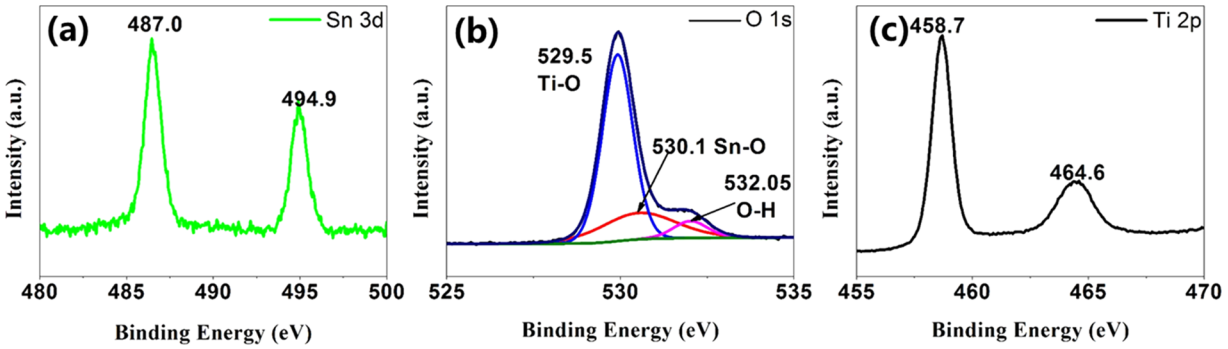

Figure 4. Patterns of (a) Sn 3d peaks, (b) O 1s peaks, and (c) Ti 2p peaks of the Sn-doped rutile TiO_2.

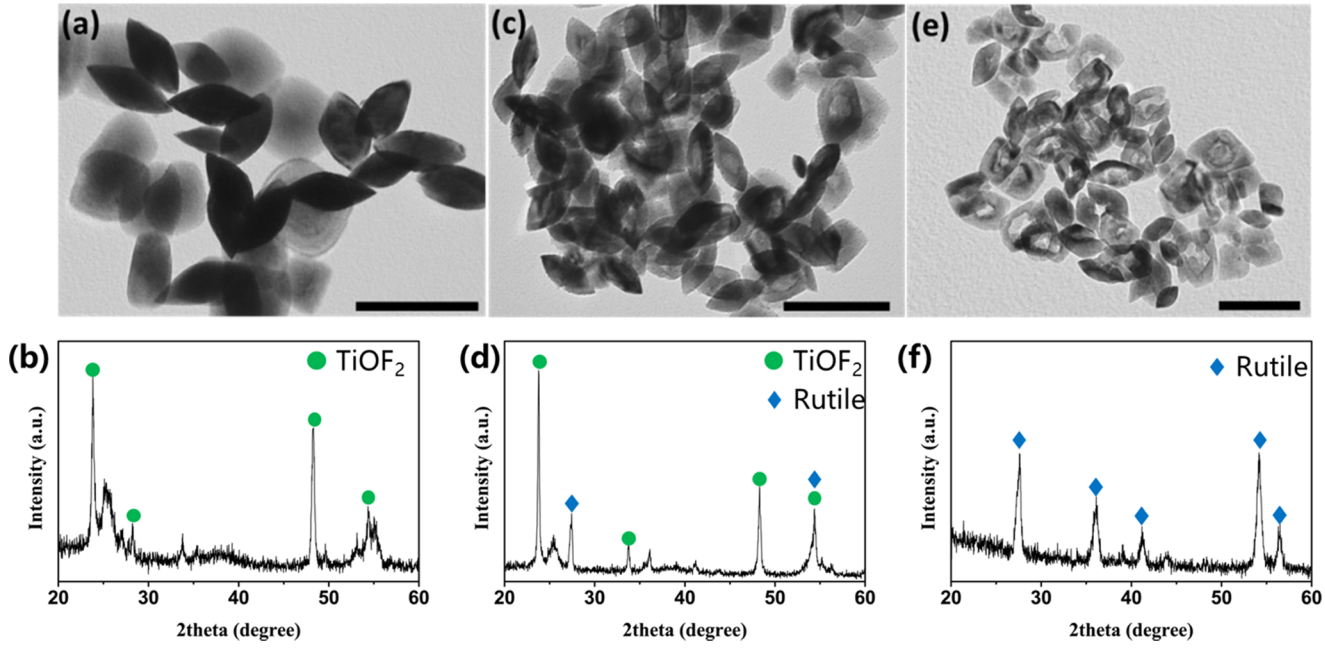

Figure 5. The TEM images and XRD patterns of the as-obtained products at different time duration: (a, b) 10 h, (c, d) 18 h, and (e, f) 24 h. The scale bar is 200 nm.

corresponding XRD patterns in Figure S2 supported the reverse transformation and the appearance of SnO_2. The quantum dots, uniformly deposited on anatase TiO_2 nanosheets, were measured by HRTEM (Figure 2f). The lattice spacing was ~0.339 nm, corresponding to the (110) plane of SnO_2. Therefore, a Sn precursor, however, with very narrow range of Sn^{4+} concentration, plays a crucial role in the formation of pure Sn-doped rutile TiO_2 hollow nanocrystals. In addition, for eliminating the effect of Cl^- for the formation of rutile TiO_2 hollow nanocrystals, several kinds of metal chlorides were introduced instead of $SnCl_4$ in this reaction. As a result, only anatase TiO_2 products could be synthesized (Figure S3), which further illustrates the effect of doping of Sn.

To further validate the Sn doping in rutile TiO_2 hollow nanocrystals, a STEM image of single nanocrystal was recorded (Figure 3a). The corresponding EDS elemental mappings were conducted to reveal the elemental composition and distribution status in the hollow nanocrystal. Figure 3b–d confirms that Sn element was homogeneously dispersed in the TiO_2 hollow nanocrystal. As mentioned above, the as-obtained rutile TiO_2 hollow nanocrystals have smooth surfaces and clear lattice fringes (Figure S4). Therefore, it can be concluded that the Sn element was well doped into the rutile TiO_2 lattice.

The molar ratio of Sn element in TiO_2 sample was 8.7%, as calculated by fitting of XPS spectra. The peaks centered at 487.0 and 494.9 eV can be indexed to Sn 3d peaks (Figure 4a),[34,35] corresponding to Sn^{4+} bound to oxygen in the Sn-doped rutile TiO_2. Because of the structural similarity between the rutile SnO_2 and TiO_2 (Figure S5 and Table S1),[10,14,36] the Sn elements would occupy a part of the Ti sites in the doping process. In Figure 4b, the slightly asymmetric spectrum of O 1s can be resolved into three peaks. The O 1s peaks centered at 529.5 and 530.1 eV can be typically assigned to Ti–O bond in the rutile TiO_2 structure[37,38] and the Sn–O bond,[31] respectively. The peak at 532.05 may result from the band of the adsorbed hydroxyl (–OH) groups on the nanomaterial surface.[31] Ti 2p peaks (Figure 4c) of the Sn-doped rutile TiO_2 show two peaks, corresponding to Ti^{4+} (Ti $2p_{1/2}$ at 464.6 eV and Ti $2p_{3/2}$ at 458.7 eV).[37−39] The UV–vis spectrum of Sn-doped rutile TiO_2 presented a narrowed band gap of ~0.1 eV compared to that of pure rutile TiO_2 (Figure S6), which was consistent with the theoretical simulation (Figures S7 and S8).

To shed light on the formation process of the rutile TiO_2 hollow nanocrystals, experiments were carried out at 200 °C for different reaction times to monitor the morphology evolution of nanoparticles. As shown in Figure 5a, solid nanocrystals were

DOI: 10.1021/acsomega.7b01340
ACS Omega 2018, 3, 1329−1337

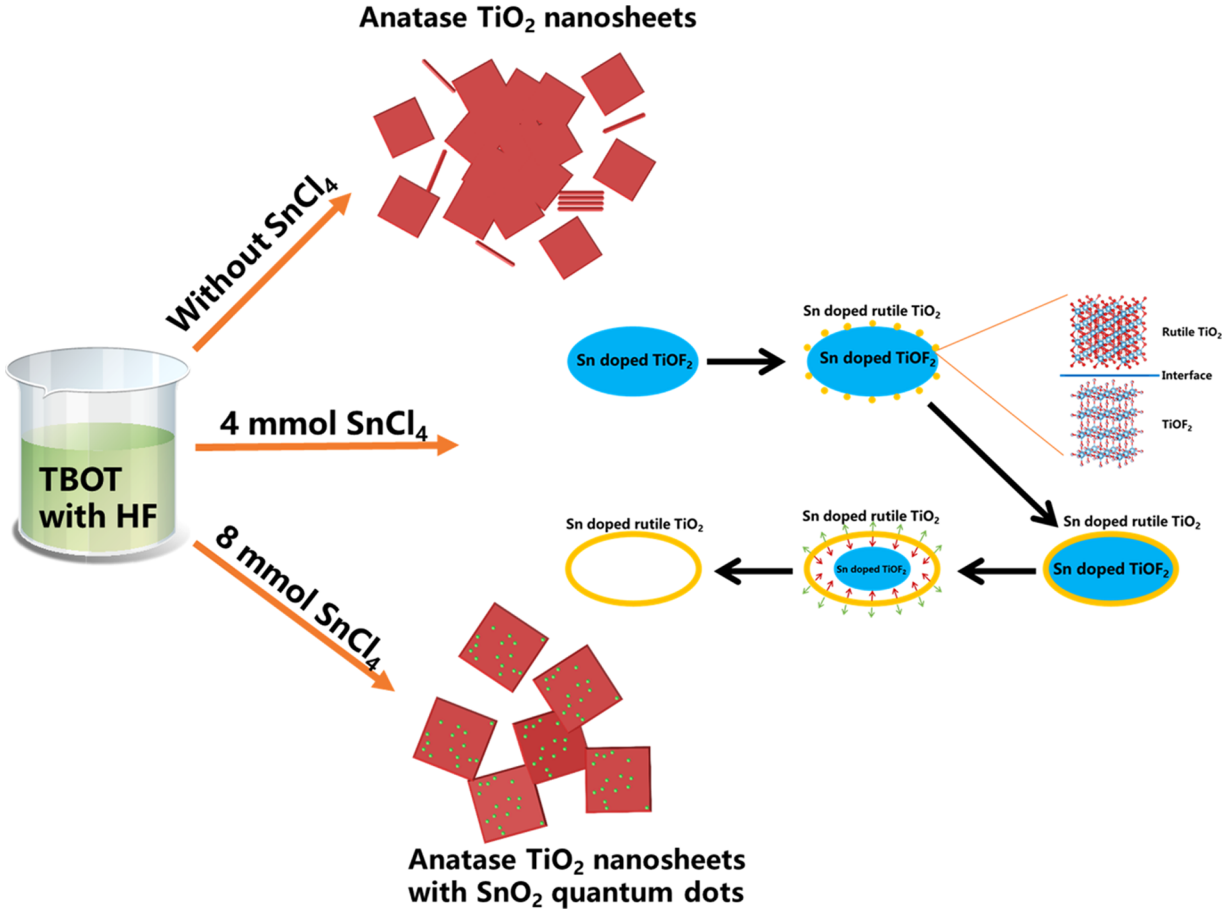

Figure 6. Schematic illustration of forming the rutile Sn-doped TiO_2 hollow nanocrystals via the template-engaged topotactic transformation process from Sn-doped $TiOF_2$ precursor.

obtained for 10 h, which were indexed to be $TiOF_2$ (JCPDS No. 08-0060) by the corresponding XRD pattern (Figure 5b). When the reaction time was extended to 18 h (Figure 5c,d), some new diffraction peaks, corresponding to the rutile TiO_2, also appeared besides the peaks of $TiOF_2$, indicating the conversion from $TiOF_2$ precursor to rutile TiO_2. This is possibly due to the hydrolysis of $TiOF_2$.[40−43] More importantly, a part of solid $TiOF_2$ nanocrystals transformed into hollow structures, which still kept the similar external morphologies. The conversion process reflected that the formation of hollow nanocrystals through in situ transformation of $TiOF_2$ precursor.[43] The phase transformation from $TiOF_2$ to rutile TiO_2 was completed within 24 h. Then, uniform TiO_2 hollow nanocrystals were obtained (Figure 5e,f).

Furthermore, a sacrificial self-template mechanism was proposed to illustrate the formation process of rutile TiO_2 hollow nanocrystals.[44,45] First, the Sn-doped $TiOF_2$ crystallites (Figures 6 and S9) were gradually hydrolyzed to form Sn-doped TiO_2 nanocrystals in a hydrothermal reaction.[42] These primary nanocrystals uniformly deposited on the surfaces of Sn-doped $TiOF_2$ crystallites (Figure S10) and then formed TiO_2 shells. Because of the restriction from the template, the as-obtained rutile TiO_2 showed the same shape with the $TiOF_2$ precursor. The TiO_2 shells became thicker with the increasing reaction time, whereas the solid $TiOF_2$ templates were continually consumed inward. Finally, the $TiOF_2$ precursor completely disappeared. Therefore, the template-engaged topotactic transformation mechanism is responsible for the formation of rutile TiO_2 hollow nanocrystals.[46,47] When no $SnCl_4$ was added in the reaction system, only anatase TiO_2 nanosheets can be obtained. Excessive $SnCl_4$ easily led to the formation of SnO_2 quantum dots instead of doping in the rutile TiO_2 hollow nanocrystals.

The lithium storage properties of the Sn-doped rutile TiO_2 hollow nanocrystals were then evaluated. Figure 7a shows the representative discharge−charge curves of the crystals during the 1st, 2nd, 5th, and 150th cycle at a voltage range from 0.01 to 3.0 V with a current rate of 0.1 A g^{-1}. Two major voltage plateaus at ∼1.4 and ∼1.0 V vs Li/Li^+ are presented in the first discharge curve, consistent with other rutile TiO_2 electrodes.[22,48] The results were also supported by the CV results (Figure S11), which are related to the Li^+ insertion into the octahedral sites of the TiO_6 octahedrons.[49] Despite the two major peaks in the CV patterns, some unknown peaks have also been observed, which are possibly derived from some side reactions in the electrode. In addition, the absence of peaks at ∼0.6 and ∼1.3 V, which are characteristic of the dealloying process of Li_xSn and the partially reversible reaction of SnO_2 with Li^+,[50−53] thus, indicates the uniform doping of tin in the rutile TiO_2 lattice. A high initial capacity of 596.9 mA h g^{-1} is exhibited in the initial discharge process, which is much higher than the theoretical capacity of the pure rutile TiO_2 ($TiO_2 + xLi + xe^- \rightarrow Li_xTiO_2$ ($x \leq 1$)).[8] The hollow structures with a high specific surface area and a large pore volume (Figure S12) and doping of tin offer more active sites for Li^+ storage.[18,54,55] In the following process, a capacity of 337.9 mA h g^{-1} was

DOI: 10.1021/acsomega.7b01340
ACS Omega 2018, 3, 1329−1337

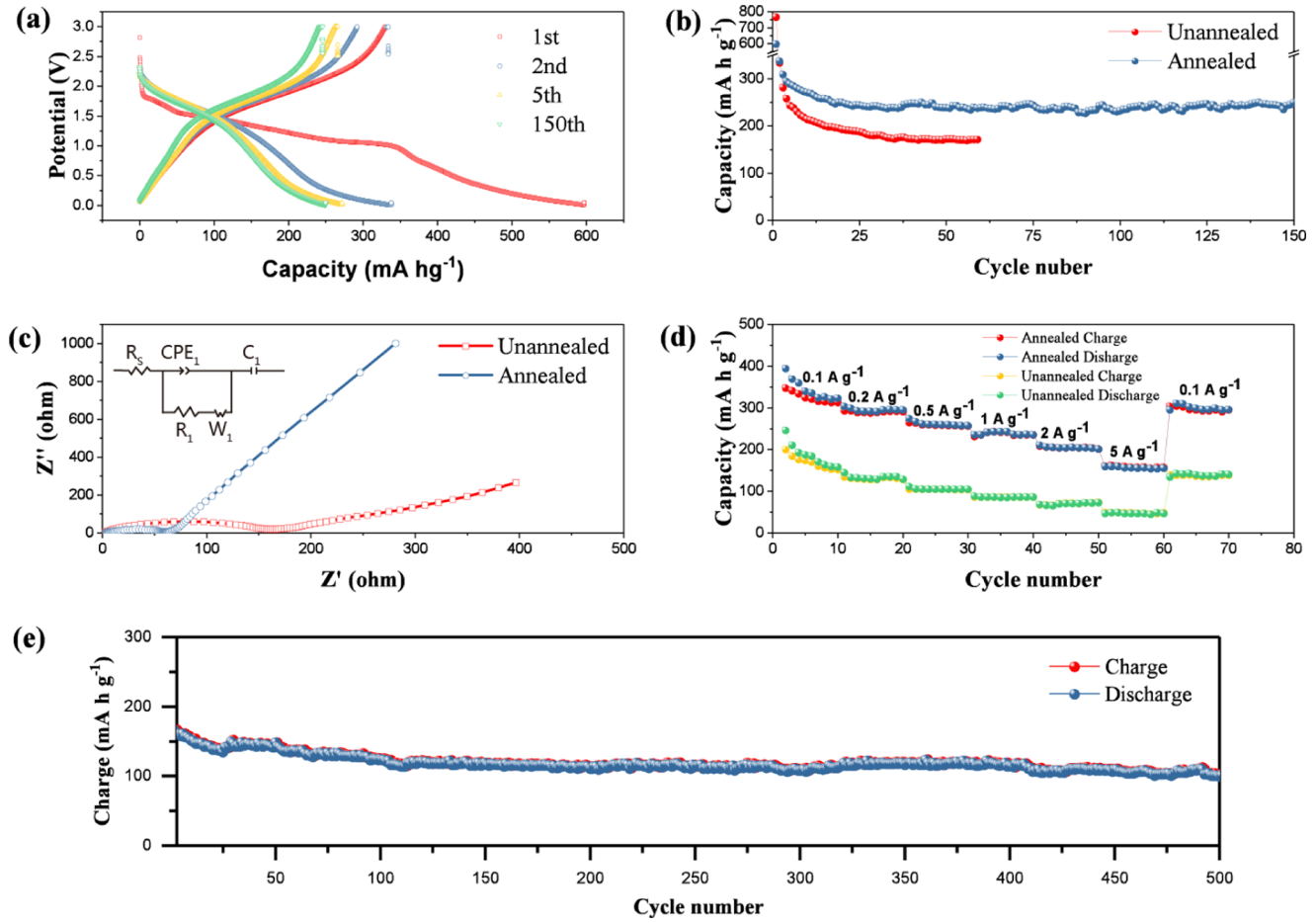

Figure 7. Electrochemical properties of the Sn-doped rutile TiO_2 sample: (a) discharge−charge curves of them during the 1st, 2nd, 5th, and 150th cycle; (b) cycle performances at 100 mA g^{-1} in the 0.01−3 V range of the annealed and unannealed Sn-doped rutile TiO_2; (c) electrochemical impedance spectroscopies of annealed and unannealed Sn-doped rutile TiO_2; (d) rate capabilities of the annealed and unannealed rutile TiO_2 at a current density ranging from 100 to 5000 mA h g^{-1}; (e) the cycling performance of annealed Sn-doped rutile TiO_2 at the rate of 5000 mA h g^{-1} (30 C, 1 C = 173 mA g^{-1}).

obtained. The irreversible capacity loss is about 43.4%. This can be derived from the deep trapping of inserted Li^+ after large volume strain in the crystal structure, as well as the formation of SEI film.[48] After the first several cycles, the specific capacity of the Sn-doped rutile TiO_2 hollow nanocrystals electrode is stabilized (Figure 7b). In the second charge/discharge cycle, a discharge capacity of 337.9 mA h g^{-1} is delivered, followed by a charge capacity of 333.9 mA h g^{-1}, leading to a high Coulombic efficiency (CE) of about 98.8%. The discharge capacity sustains at about 251.3 mA h g^{-1} after 150 cycles at a current rate of 0.1 A g^{-1}, which is superior to most other nanostructured rutile TiO_2-based anode materials (Table S2). Because SnO_2 has a higher theoretical capacity than TiO_2, Sn^{4+} doping in the rutile TiO_2 lattice naturally leads to an enhanced reversible capacity ($Li^+ + SnO_2 \rightarrow Sn + Li_2O$; $Sn + xLi \rightarrow Li_xSn$ ($x < 4.4$)).[51,53] In addition, annealing treatment also benefited the increase in Li^+ storage property in the prepared Sn-doped TiO_2 hollow nanocrystals (Figure 7b). This is due to the improved crystallinity and absence of side reactions, related with the oxygen vacancies, after annealing. In comparison, the undoped TiO_2 nanosheets were also synthesized via a similar hydrothermal method without $SnCl_4$ in the reaction system, which exhibited inferior electrochemical activity (Figure S13). Electrochemical impedance spectroscopy (EIS) measurement is carried out to study the charge-transfer impedance of Sn-doped rutile TiO_2 hollow nanocrystals electrode (Figure 7c). The Nyquist plots of the annealed and unannealed hollow nanocrystals are obtained with the amplitude of 5 mV and a frequency ranging from 0.01 Hz to 100 kHz. It is clear that the semicircle of the annealed Sn-doped rutile TiO_2 hollow nanocrystals is smaller than that of the unannealed ones, demonstrating a smaller solid-state interface resistance of the sample after annealing. Inset in Figure 7c shows an equivalent circuit. The small intercept (R_s) at the Z' axis represents the total resistance of the electrolyte, separator, and electrical contacts.[53] The semicircle corresponds to R_1, representing charge-transfer impedance on the electrode−electrolyte interface.[4] The sloping line, corresponding to W (Warburg impedance), indicates the diffusion of Li^+ into the active materials.[2] The CPE_1 is the constant phase-angle element, involving double-layer capacitance, which is relevant with the surface property of the electrode.[52] C_1 represents the capacitance caused by Li^+ transport process in the electrode material.[16] The R_1 of annealed Sn-doped TiO_2 hollow nanocrystals was 64.11 Ω cm^{-2}, which is much smaller than that of unannealed electrode (160.9 Ω cm^{-2}) and means well charge transport property on the electrode−electrolyte surface. It is due to the doping of Sn^{4+} and high crystallinity. The improved conductivity benefits the electrons and Li^+ transport in the electrode.[8] Meanwhile, the hollow nanostructures can

DOI: 10.1021/acsomega.7b01340
ACS Omega 2018, 3, 1329−1337

offer more sites for ions insertion. Therefore, a high specific capacity can be expected.

The excellent rate behavior of the sample was further investigated at different current rates (0.1−5 A g^{-1}; Figure 7d). Ten charge/discharge cycles were tested at each step from 0.1 to 5 A g^{-1}. Obviously, the Sn-doped rutile TiO_2 hollow nanocrystals exhibited much more improved rate performances than unannealed sample at each current rate. The specific capacities for Sn-doped rutile TiO_2 hollow nanocrystals are 313.4, 291.4, 256.5, 235.5, and 201.4 mA h g^{-1} at the rate of 0.1, 0.2, 0.5, 1, and 2 A g^{-1}, respectively. Moreover, even at the highest current of 5 A g^{-1}, a high capacity of 155.6 mA h g^{-1} is still obtained. Furthermore, the capacity can be returned to the initial value of 295.6 mA h g^{-1} after measuring at high current rate of 30 C, indicating their good structural stability. To evaluate the cyclability at a high current rate, the Sn-doped rutile TiO_2 hollow nanocrystals electrode was discharged−charged at 30 C over 500 cycles. It is clear that this sample retained a reversible capacity of ∼110 mA h g^{-1} after 500 cycles at about 30 C (Figure 7e). The CE remained almost 100% during the 500 cycles, indicating excellent stability of the electrode. More importantly, the hollow structure of Sn-doped rutile TiO_2 nanocrystals was well maintained after 100 cycles under 1 A g^{-1}, which further illuminates the stability of the electrode[56] (Figure S14). In comparison with the reported rutile TiO_2, the Sn-doped rutile TiO_2 hollow nanocrystals exhibited significant rate capabilities and cycling stability (Table S2).

4. CONCLUSIONS

In summary, Sn-doped rutile TiO_2 hollow nanocrystals were successfully synthesized by a facile hydrothermal method. The hollow nanostructures were transformed from solid $TiOF_2$ nanocrystals by hydrolysis. Owing to tin doping, uniform hollow structure, and high crystallinity, the TiO_2 products demonstrated remarkable rate capabilities and excellent long-life cycling stability at a high current rate. They delivered a high reversible specific capacity of 251.3 mA h g^{-1} at the current rate of 0.1 A g^{-1}. Moreover, they still exhibited as high as ∼110 mA h g^{-1} over 500 cycles at the current rate of 5 A g^{-1} (30 C). These electrochemical performances are superior to those of most rutile TiO_2 reported so far. Therefore, it is expected that the Sn-doped rutile TiO_2 hollow nanocrystals will be a potential candidate as the anode material.

■ ASSOCIATED CONTENT

Supporting Information

The Supporting Information is available free of charge on the ACS Publications website at DOI: 10.1021/acsomega.7b01340.

Figures S1−S14; Tables S1 and S2; references (PDF)

■ AUTHOR INFORMATION

Corresponding Authors

*E-mail: liangang@sdu.edu.cn (G.L.).
*E-mail: cuidl@sdu.edu.cn (D.C.).
*E-mail: cpwong@cuhk.edu.hk (C.-P.W.).

ORCID

Ching-Ping Wong: 0000-0003-3556-8053

Author Contributions

‖S.J. and G.L. contributed equally.

Author Contributions

The manuscript was written through contributions of all of the authors. All of the authors have given approval to the final version of the manuscript.

Notes

The authors declare no competing financial interest.

■ ACKNOWLEDGMENTS

This work was supported by NSFC (grant numbers 51372143, 51102151, and 50990061) and Natural Science Foundation of Shandong Province (2013GGX10208).

■ REFERENCES

(1) Malik, R.; Zhou, F.; Ceder, G. Kinetics of Non-Equilibrium Lithium Incorporation in $LiFePO_4$. *Nat. Mater.* **2011**, *10*, 587−590.

(2) Yang, L.; Wang, S.; Mao, J.; Deng, J.; Gao, Q.; Tang, Y.; Schmidt, O. G. Hierarchical MoS2/polyaniline Nanowires with Excellent Electrochemical Performance for Lithium-Ion Batteries. *Adv. Mater.* **2013**, *25*, 1180−1184.

(3) Myung, S.-T.; Kikuchi, M.; Yoon, C. S.; Yashiro, H.; Kim, S.-J.; Sun, Y.-K.; Scrosati, B. Black Anatase Titania Enabling Ultra High Cycling Rates for Rechargeable Lithium Batteries. *Energy Environ. Sci.* **2013**, *6*, 2609.

(4) Chen, X.; Li, C.; Grätzel, M.; Kostecki, R.; Mao, S. S. Nanomaterials for Renewable Energy Production and Storage. *Chem. Soc. Rev.* **2012**, *41*, 7909.

(5) Song, T.; Paik, U. TiO_2 as an Active or Supplemental Material for Lithium Batteries. *J. Mater. Chem. A* **2016**, *4*, 14−31.

(6) Wang, S.; Guan, B. Y.; Yu, L.; Lou, X. W. D. Rational Design of Three-Layered TiO_2@Carbon@MoS_2 Hierarchical Nanotubes for Enhanced Lithium Storage. *Adv. Mater.* **2017**, *29*, No. 1702724.

(7) Guan, B. Y.; Yu, L.; Li, J.; Lou, X. W. (David). A Universal Cooperative Assembly-Directed Method for Coating of Mesoporous TiO_2 Nanoshells with Enhanced Lithium Storage Properties. *Sci. Adv.* **2016**, *2*, No. e1501554.

(8) Jiao, W.; Li, N.; Wang, L.; Wen, L.; Li, F.; Liu, G.; Cheng, H.-M. High-Rate Lithium Storage of Anatase TiO_2 Crystals Doped with Both Nitrogen and Sulfur. *Chem. Commun.* **2013**, *49*, 3461−3463.

(9) Liu, G.; Yang, H. G.; Pan, J.; Yang, Y. Q.; Lu, G. Q. M.; Cheng, H. M. Titanium Dioxide Crystals with Tailored Facets. *Chem. Rev.* **2014**, *114*, 9559−9612.

(10) De Angelis, F.; Di Valentin, C.; Fantacci, S.; Vittadini, A.; Selloni, A. Theoretical Studies on Anatase and Less Common TiO_2 phases: Bulk, Surfaces, and Nanomaterials. *Chem. Rev.* **2014**, *114*, 9708−9753.

(11) Ramamoorthy, M.; Vanderbilt, D.; King-Smith, R. D. First-Principles Calculations of the Energetics of Stoichiometric TiO_2 Surfaces. *Phys. Rev. B* **1994**, *49*, 16721−16727.

(12) Parker, R. A.; Wasilik, J. H. Dielectric Constant and Dielectric Loss of TiO_2 (Rutile) at Low Frequencies. *Phys. Rev.* **1960**, *120*, 1631−1637.

(13) Wang, Y.-Q.; Gu, L.; Guo, Y.-G.; Li, H.; He, X.-Q.; Tsukimoto, S.; Ikuhara, Y.; Wan, L.-J. Rutile-TiO_2 Nanocoating for a High-Rate $Li_4Ti_5O_{12}$ Anode of a Lithium-Ion Battery. *J. Am. Chem. Soc.* **2012**, *134*, 7874−7879.

(14) Gligor, F.; de Leeuw, S. W. Lithium Diffusion in Rutile Structured Titania. *Solid State Ionics* **2006**, *177*, 2741−2746.

(15) Wang, S.; Yang, Y.; Quan, W.; Hong, Y.; Zhang, Z.; Tang, Z.; Li, J. Ti3+-Free Three-Phase $Li_4Ti_5O_{12}$/TiO_2 for High-Rate Lithium Ion Batteries: Capacity and Conductivity Enhancement by Phase Boundaries. *Nano Energy* **2017**, *32*, 294−301.

(16) Li, X.; Wu, G.; Liu, X.; Li, W.; Li, M. Orderly Integration of Porous TiO_2(B) Nanosheets into Bunchy Hierarchical Structure for High-Rate and Ultralong-Lifespan Lithium-Ion Batteries. *Nano Energy* **2017**, *31*, 1−8.

DOI: 10.1021/acsomega.7b01340
ACS Omega 2018, 3, 1329−1337

(17) Xin, X.; Zhou, X.; Wu, J.; Yao, X.; Liu, Z. Scalable Synthesis of TiO_2/graphene Nanostructured Composite with High-Rate Performance for Lithium Ion Batteries. *ACS Nano* **2012**, *6*, 11035−11043.
(18) Zhang, G.; Wu, H.; Bin; Song, T.; Paik, U.; Lou, X. W. TiO_2 Hollow Spheres Composed of Highly Crystalline Nanocrystals Exhibit Superior Lithium Storage Properties. *Angew. Chem., Int. Ed.* **2014**, *53*, 12590−12593.
(19) Li, D.; Qin, Q.; Duan, X.; Yang, J.; Guo, W.; Zheng, W. General One-Pot Template-Free Hydrothermal Method to Metal Oxide Hollow Spheres and Their Photocatalytic Activities and Lithium Storage Properties. *ACS Appl. Mater. Interfaces* **2013**, *5*, 9095−9100.
(20) Fang, W. Q.; Huo, Z.; Liu, P.; Wang, X. L. u; Zhang, M.; Jia, Y.; Zhang, H.; Zhao, H.; Yang, H. G.; Yao, X. Fluorine-Doped Porous Single-Crystal Rutile TiO_2 Nanorods for Enhancing Photoelectrochemical Water Splitting. *Chemistry* **2014**, *20*, 11439−11444.
(21) Usui, H.; Yoshioka, S.; Wasada, K.; Shimizu, M.; Sakaguchi, H. Nb-Doped Rutile TiO_2: A Potential Anode Material for Na-Ion Battery. *ACS Appl. Mater. Interfaces* **2015**, *7*, 6567−6573.
(22) Chen, J.; Song, W.; Hou, H.; Zhang, Y.; Jing, M.; Jia, X.; Ji, X. Ti3+ Self-Doped Dark Rutile TiO_2 Ultrafine Nanorods with Durable High-Rate Capability for Lithium-Ion Batteries. *Adv. Funct. Mater.* **2015**, 6793−6801.
(23) Tian, H.; Xin, F.; Tan, X.; Han, W. High Lithium Electroactivity of Boron-Doped Hierarchical Rutile Submicrosphere TiO_2. *J. Mater. Chem. A* **2014**, *2*, 10599−10606.
(24) Zhang, W.; Zhou, W.; Wright, J. H.; Kim, Y. N.; Liu, D.; Xiao, X. Mn-Doped TiO_2 Nanosheet-Based Spheres as Anode Materials for Lithium-Ion Batteries with High Performance at Elevated Temperatures. *ACS Appl. Mater. Interfaces* **2014**, *6*, 7292−7300.
(25) Wang, H.; Xi, L.; Tucek, J.; Ma, C.; Yang, G.; Leung, M. K. H.; Zboril, R.; Niu, C.; Rogach, A. L. Synthesis and Characterization of Tin Titanate Nanotubes: Precursors for Nanoparticulate Sn-Doped TiO_2 Anodes with Synergistically Improved Electrochemical Performance. *ChemElectroChem* **2014**, *1*, 1563−1569.
(26) Wang, Y.; Smarsly, B. M.; Djerdj, I. Niobium Doped TiO_2 with Mesoporosity and Its Application for Lithium Insertion. *Chem. Mater.* **2010**, *22*, 6624−6631.
(27) Lan, T.; Zhang, W.; Wu, N.-L.; Wei, M. Nb-Doped Rutile TiO_2 Mesocrystals with Enhanced Lithium Storage Properties for Lithium Ion Battery. *Chem. - Eur. J.* **2017**, *23*, 5059−5065.
(28) Zhou, X.; Wan, L. J.; Guo, Y. G. Binding SnO_2 Nanocrystals in Nitrogen-Doped Graphene Sheets as Anode Materials for Lithium-Ion Batteries. *Adv. Mater.* **2013**, *25*, 2152−2157.
(29) Guan, C.; Wang, X.; Zhang, Q.; Fan, Z.; Zhang, H.; Fan, H. J. Highly Stable and Reversible Lithium Storage in SnO_2 Nanowires Surface Coated with a Uniform Hollow Shell by Atomic Layer Deposition. *Nano Lett.* **2014**, *14*, 4852−4858.
(30) Sang, L.; Zhao, Y.; Burda, C. TiO_2 Nanoparticles as Functional Building Blocks. *Chem. Rev.* **2014**, *114*, 9283−9318.
(31) Jing, L. Y.; Fu, A. P.; Li, H. L.; Liu, J. Q.; Guo, P. Z.; Wang, Y. Q.; Zhao, X. S. One-Step Solvothermal Preparation of Fe_3O_4/graphene Composites at Elevated Temperature and Their Application as Anode Materials for Lithium-Ion Batteries. *RSC Adv.* **2014**, *4*, 59981−59989.
(32) Wang, H.; Xi, L.; Tucek, J.; Zhan, Y.; Hung, T. F.; Kershaw, S. V.; Zboril, R.; Chung, C. Y.; Rogach, A. L. Hierarchical Assembly of Ti(IV)/Sn(II) Co-Doped SnO_2 Nanosheets along Sacrificial Titanate Nanowires: Synthesis, Characterization and Electrochemical Properties. *Nanoscale* **2013**, *5*, 9101−9109.
(33) Shannon, R. D. Revised Effective Ionic Radii and Systematic Studies of Interatomic Distances in Halides and Chalcogenides. *Acta Crystallogr., Sect. A: Found. Adv.* **1976**, *32*, 751−767.
(34) Wang, X.; Cao, X.; Bourgeois, L.; Guan, H.; Chen, S.; Zhong, Y.; Tang, D.-M.; Li, H.; Zhai, T.; Li, L.; Bando, Y.; Golberg, D. N-Doped Graphene-SnO_2 Sandwich Paper for High-Performance Lithium-Ion Batteries. *Adv. Funct. Mater.* **2012**, *22*, 2682−2690.
(35) Ding, L.; He, S.; Miao, S.; Jorgensen, M. R.; Leubner, S.; Yan, C.; Hickey, S. G.; Eychmüller, A.; Xu, J.; Schmidt, O. G. Ultrasmall SnO_2 Nanocrystals: Hot-Bubbling Synthesis, Encapsulation in Carbon Layers and Applications in High Capacity Li-Ion Storage. *Sci. Rep.* **2014**, *4*, No. 4647.
(36) Miiller, W.; Kearley, G. J.; Ling, C. D. Ab Initio Parametrized Polarizable Force Field for Rutile-Type SnO_2. *Theor. Chem. Acc.* **2012**, *131*, 1216.
(37) Gordon, T. R.; Cargnello, M.; Paik, T.; Mangolini, F.; Weber, R. T.; Fornasiero, P.; Murray, C. B. Nonaqueous Synthesis of TiO_2 Nanocrystals Using TiF_4 to Engineer Morphology, Oxygen Vacancy Concentration, and Photocatalytic Activity. *J. Am. Chem. Soc.* **2012**, *134*, 6751−6761.
(38) Etacheri, V.; Yourey, J. E.; Bartlett, B. M. Chemically Bonded TiO_2-Bronze Nanosheet/reduced Graphene Oxide Hybrid for High-Power Lithium Ion Batteries. *ACS Nano* **2014**, *8*, 1491−1499.
(39) Yuan, Q.; Wu, Z.; Jin, Y.; Xu, L.; Xiong, F.; Ma, Y.; Huang, W. Photocatalytic Cross-Coupling of Methanol and Formaldehyde on a Rutile TiO_2(110) Surface. *J. Am. Chem. Soc.* **2013**, *135*, 5212−5219.
(40) Goriparti, S.; Miele, E.; Prato, M.; Scarpellini, A.; Marras, S.; Monaco, S.; Toma, A.; Messina, G. C.; Alabastri, A.; De Angelis, F.; Manna, L.; Capiglia, C.; Zaccaria, R. P. Direct Synthesis of Carbon-Doped TiO_2-Bronze Nanowires as Anode Materials for High Performance Lithium-Ion Batteries. *ACS Appl. Mater. Interfaces* **2015**, *7*, 25139−25146.
(41) Ding, X.; Hong, Z.; Wang, Y.; Lai, R.; Wei, M. Synthesis of Square-like Anatase TiO_2 Nanocrystals Based on $TiOF_2$ Quantum Dots. *J. Alloys Compd.* **2013**, *550*, 475−478.
(42) Huang, Z.; Wang, Z.; Lv, K.; Zheng, Y.; Deng, K. Transformation of $TiOF_2$ Cube to a Hollow Nanobox Assembly from Anatase TiO_2 Nanosheets with Exposed {001} Facets via Solvothermal Strategy. *ACS Appl. Mater. Interfaces* **2013**, *5*, 8663−8669.
(43) Wang, Z. Y.; Huang, B. B.; Dai, Y.; Zhang, X. Y.; Qin, X. Y.; Li, Z.; Zheng, Z. K.; Cheng, H. F.; Guo, L. W. Topotactic Transformation of Single-Crystalline TiOF2 Nanocubes to Ordered Arranged 3D Hierarchical TiO_2 Nanoboxes. *CrystEngComm* **2012**, *14*, 4578−4581.
(44) Yang, J.; Qi, L.; Lu, C.; Ma, J.; Cheng, H. Morphosynthesis of Rhombododecahedral Silver Cages by Self-Assembly Coupled with Precursor Crystal Templating. *Angew. Chem., Int. Ed.* **2005**, *44*, 598−603.
(45) Jiao, S.; Xu, L.; Jiang, K.; Xu, D. Well-Defined Non-Spherical Copper Sulfide Mesocages with Single-Crystalline Shells by Shape-Controlled Cu_2O Crystal Templating. *Adv. Mater.* **2006**, *18*, 1174−1177.
(46) Li, L.; Sun, N.; Huang, Y.; Qin, Y.; Zhao, N.; Gao, J.; Li, M.; Zhou, H.; Qi, L. Topotactic Transformation of Single-Crystalline Precursor Discs into Disc-like Bi2S3 Nanorod Networks. *Adv. Funct. Mater.* **2008**, *18*, 1194−1201.
(47) Guo, C. F.; Cao, S.; Zhang, J.; Tang, H.; Guo, S.; Tian, Y.; Liu, Q. Topotactic Transformations of Superstructures: From Thin Films to Two-Dimensional Networks to Nested Two-Dimensional Networks. *J. Am. Chem. Soc.* **2011**, *133*, 8211−8215.
(48) Yu, X.-Y.; Wu, H. B.; Yu, L.; Ma, F.-X.; Lou, X. W. D. Rutile TiO_2 Submicroboxes with Superior Lithium Storage Properties. *Angew. Chem., Int. Ed.* **2015**, *54*, 4001−4004.
(49) Long, L.; Zhang, H.; Ye, M.; Fang, Z. Ammonia Cation-Assisted Bubble Template for Synthesizing Hollow TiO_2 Nanospheres and Their Application in Lithium Ion Storage. *RSC Adv.* **2015**, *5*, 12224−12229.
(50) Chen, J. S.; Lou, X. W. D. SnO_2 -Based Nanomaterials: Synthesis and Application in Lithium-Ion Batteries. *Small* **2013**, *9*, 1877−1893.
(51) Guan, C.; Wang, X.; Zhang, Q.; Fan, Z.; Zhang, H.; Fan, H. J. Highly Stable and Reversible Lithium Storage in SnO_2 Nanowires Surface Coated with a Uniform Hollow Shell by Atomic Layer Deposition. *Nano Lett.* **2014**, *14*, 4852−4858.
(52) Yang, S.; Yue, W.; Zhu, J.; Ren, Y.; Yang, X. Graphene-Based Mesoporous SnO_2 with Enhanced Electrochemical Performance for Lithium-Ion Batteries. *Adv. Funct. Mater.* **2013**, *23*, 3570−3576.
(53) Lin, J.; Peng, Z.; Xiang, C.; Ruan, G.; Yan, Z.; Natelson, D.; Tour, J. M. Graphene Nanoribbon and Nanostructured SnO_2

DOI: 10.1021/acsomega.7b01340
ACS Omega 2018, 3, 1329−1337

Composite Anodes for Lithium Ion Batteries. *ACS Nano* **2013**, *7*, 6001−6006.
(54) Ren, H.; Yu, R.; Wang, J.; Jin, Q.; Yang, M.; Mao, D.; Kisailus, D.; Zhao, H.; Wang, D. Multishelled TiO_2 Hollow Microspheres as Anodes with Superior Reversible Capacity for Lithium Ion Batteries. *Nano Lett.* **2014**, *14*, 6679−6684.
(55) Wang, Z.; Zhou, L.; Lou, X. W. Metal Oxide Hollow Nanostructures for Lithium-Ion Batteries. *Adv. Mater.* **2012**, *24*, 1903−1911.
(56) Han, C.; Yang, D.; Yang, Y.; Jiang, B.; He, Y.; Wang, M.; Song, A.-Y.; He, Y.-B.; Li, B.; Lin, Z. Hollow Titanium Dioxide Spheres as Anode Material for Lithium Ion Battery with Largely Improved Rate Stability and Cycle Performance by Suppressing the Formation of Solid Electrolyte Interface Layer. *J. Mater. Chem. A* **2015**, *3*, 13340−13349.

DOI: 10.1021/acsomega.7b01340
ACS Omega 2018, 3, 1329−1337